

# Deflecting Dendrites by Introducing Compressive Stress in $\text{Li}_7\text{La}_3\text{Zr}_2\text{O}_{12}$ Using Ion Implantation

Florian Flatscher, Juraj Todt, Manfred Burghammer, Hanne-Sofie Søreide, Lukas Porz, Yanjun Li, Sigurd Wenner, Viktor Bobal, Steffen Ganschow, Bernhard Sartory, Roland Brunner, Constantinos Hatzoglou, Jozef Keckes, and Daniel Rettenwander\*

Lithium dendrites belong to the key challenges of solid-state battery research. They are unavoidable due to the imperfect nature of surfaces containing defects of a critical size that can be filled by lithium until fracturing the solid electrolyte. The penetration of Li metal occurs along the propagating crack until a short circuit takes place. It is hypothesized that ion implantation can be used to introduce stress states into  $\text{Li}_{6.4}\text{La}_3\text{Zr}_{1.4}\text{Ta}_{0.6}\text{O}_{12}$  which enables an effective deflection and arrest of dendrites. The compositional and microstructural changes associated with the implantation of Ag-ions are studied via atom probe tomography, electron microscopy, and nano X-ray diffraction indicating that Ag-ions can be implanted up to 1  $\mu\text{m}$  deep and amorphization takes place down to 650–700 nm, in good agreement with kinetic Monte Carlo simulations. Based on diffraction results pronounced stress states up to  $-700 \text{ MPa}$  are generated in the near-surface region. Such a stress zone and the associated microstructural alterations exhibit the ability to not only deflect mechanically introduced cracks but also dendrites, as demonstrated by nano-indentation and galvanostatic cycling experiments with subsequent electron microscopy observations. These results demonstrate ion implantation as a viable technique to design “dendrite-free” solid-state electrolytes for high-power and energy-dense solid-state batteries.

## 1. Introduction

Lithium metal has been the holy grail of anode materials for Li batteries, since the first usage in the 1960s, boasting the highest theoretical capacity at  $3860 \text{ mAh g}^{-1}$ , the lowest possible electrochemical potential,  $-3.04 \text{ V}$  versus standard hydrogen electrode, and a low mass density.<sup>[1–4]</sup> Despite its desirable parameters, safety issues stemming from dendritic growth of lithium, short-circuiting, and subsequent ignition of the liquid electrolyte, have led to its replacement by the graphite anode in commercial lithium-ion batteries.<sup>[1–4]</sup> Through the usage of non-flammable solid electrolytes which are compatible with lithium metal, such as the oxide garnet  $\text{Li}_7\text{La}_3\text{Zr}_2\text{O}_{12}$  (LLZO), safety concerns can be remedied and a resurgence of the lithium metal anode is possible.<sup>[5,6]</sup>

The problem of dendritic growth remains though, still present in solid electrolytes, which are prone to being cracked

F. Flatscher, H.-S. Søreide, L. Porz, Y. Li, C. Hatzoglou, D. Rettenwander  
Department of Materials Science and Engineering

NTNU Norwegian University of Science and Technology  
Trondheim 7491, Norway  
E-mail: daniel.rettenwander@ntnu.no

F. Flatscher, D. Rettenwander  
Christian Doppler Laboratory for Solid-State Batteries  
NTNU Norwegian University of Science and Technology  
Trondheim 7491, Norway

J. Todt, J. Keckes  
Chair of Materials Physics  
Montanuniversität Leoben and Erich Schmid  
Institute for Materials Science  
Austrian Academy of Sciences  
Leoben 8700, Austria

M. Burghammer  
European Synchrotron Radiation Facility  
6 rue Jules Horowitz, BP220, Grenoble, cedex 9 38043, France

S. Wenner  
SINTEF Industry  
Department of Materials and Nanotechnology  
Trondheim 7465, Norway

V. Bobal  
Department of Physics  
University of Oslo  
Oslo 0316, Norway

S. Ganschow  
Leibniz-Institut für Kristallzüchtung  
Berlin Germany  
B. Sartory, R. Brunner  
Materials Center Leoben  
Leoben 8700, Austria

© 2023 The Authors. Small published by Wiley-VCH GmbH. This is an open access article under the terms of the Creative Commons Attribution License, which permits use, distribution and reproduction in any medium, provided the original work is properly cited.

DOI: 10.1002/smll.202307515

by lithium dendrites, even when the material is mechanically stronger than lithium metal. This can happen at current densities as low as  $0.1 \text{ mA cm}^{-2}$  at room temperature.<sup>[7–9]</sup> The precise mechanism of dendrite formation in solid electrolytes is far from fully explored but one explanation is that inhomogeneous current distribution, sometimes named current focusing, leads to preferential lithium plating, accelerating the build-up of mechanical stress in the ceramic until it is released in fracture of the material.<sup>[10–13]</sup>

Recently it was found that directed stresses in the material allow for guiding the growing crack in a certain direction. With increasing in plane compressive stress, the path of the growing crack aligns more and more with the stress direction, depending on the initial crack angle, as the path of least resistance from the mechanical perspective diverges from the electrochemical one. It was shown that if the stress is high enough, at least in the 200 MPa range for LLZO, cracks can be diverted to a  $90^\circ$  angle from the surface regardless of the initial crack direction. This can stop the dendrite from reaching the opposite electrode and short-circuiting the cell.<sup>[14]</sup> In the work described, the stress was applied through mechanical bending of the solid electrolyte via a cantilever. Since bending a whole battery pack is rather impractical, the introduction of residual stress is necessary. Theoretical work also shows that this residual stress in LLZO should be able to inhibit dendrites.<sup>[15]</sup>

There are a few methods to introduce residual stresses, which is also known to increase the fracture resistance, depending on the type of stress introduced into a material. In metallurgy residual stresses are introduced during plastic deformation of the material, which is known as work hardening, if it occurs heterogeneously throughout the material. Work hardening can be used to significantly increase the hardness of the substrate by increasing the defect density in the material.<sup>[16]</sup> It can in principle be applied to any crystalline material, though it depends on the ductility. While metals can be deformed to introduce stresses, the same approach would shatter brittle ceramics, which LLZO counts as. This disallows the use of large-scale plastic deformation like cold rolling and special care has to be taken when introducing residual stresses using methods, such as shot peening, laser shock peening, or sand blasting in order to keep the material intact.<sup>[17–21]</sup> Other possible methods include strengthening via grain boundaries, transformation hardening, second-phase hardening, and solid solution strengthening.<sup>[22]</sup> To achieve a solid solution in a ceramic, a proven method from the semiconductor industry can be used to introduce foreign ions into the matrix, ion implantation.<sup>[23–25]</sup> Previous research on different ceramics, such as MgO, Al<sub>2</sub>O<sub>3</sub>, and SiC has shown that an ion-implanted material can exhibit a higher fracture toughness.<sup>[25,26]</sup>

The implantation of ions has a multitude of effects on the material properties, depending on the used parameters. With a high enough dose of the implanted ions or beam power, the collisions of the ions with the lattice can destabilize it, leaving behind an amorphous layer in its wake.<sup>[24–25]</sup> Both of those parameters also determine the penetration depth than can be reached. This amorphized layer can even be mechanically weaker than the starting material.<sup>[25]</sup> The conductive properties of the material can also be influenced due to the implantation. Implanted ions can create additional states in the band structure changing the electronic conductivity, which made semiconductor applications possible

and is the main reason for its use.<sup>[27]</sup> If the material is amorphized, pathways for ionic conduction can be diminished, which for battery applications is rather detrimental. Nevertheless, amorphous LLZO in thin film batteries has already been reported to reach reasonably high current densities ( $3.2 \text{ mA cm}^{-2}$ ) without dendrite growth. There the thickness of the layer (70 nm) overcomes the diminished ionic conductivity of 4 orders of magnitude compared to bulk crystalline LLZO.<sup>[28]</sup> In the semiconductor industry annealing processes are typically used to regain the crystallinity and to benefit only from the increased electronic conduction without having to worry about an inhomogeneous distribution in the amorphous structure.<sup>[23]</sup> Parameters to achieve a similar reconstruction of the lattice, known as recrystallization, while keeping ion migration low, are not known yet in literature for solid electrolytes in general and LLZO specifically.

Contrary to the semiconductor industry, with thin finely polished single crystalline wafers, processing of polycrystalline material would be preferred for battery purposes to keep costs low and production volume high. This means grain boundaries and natural defects need to be kept in mind. A shallow implantation depth can run into orientation effects, leading to an inhomogeneous implantation profile similar to the implantation into non-planar semiconductors.<sup>[29]</sup> A defect which extends past the implanted zone can also be filled with lithium and bypass the deflective properties from the stress field generated by the implanted ions.

In a recent publication<sup>[30]</sup> it was shown that ion implantation is possible for solid electrolytes and given a tentative stress value of  $-3\text{--}20 \text{ GPa}$  in LLZO, depending on the dosage of implanted Xe ions, retrieved from the examination of grazing incidence X-ray diffraction (XRD) data and molecular dynamics simulations. It has to be noted that the implantation depth in Yao et al is rather shallow, calculated at up to 60 nm, and is below the common defect size in the sub  $\mu\text{m}$  size, as also mentioned by Yao et al. Furthermore, in situ plating of lithium in a transmission electron microscopy (TEM) measurement showed fracture of “defect free” single crystalline LLZO from the local stresses generated by lithium ions, reaching up to GPa levels.<sup>[31]</sup>

This study reveals that stress states in the near surface region up to 1  $\mu\text{m}$  depth and up to  $-700 \text{ MPa}$  can be introduced into Li<sub>6.4</sub>La<sub>3</sub>Zr<sub>1.4</sub>Ta<sub>0.6</sub>O<sub>12</sub> (LLZTO) by ion implantation. Such a high stress is introduced by an Ag-ion concentration lower than 0.003 at% in the LLZTO matrix and accompanied by the amorphization of the top 650–700 nm of LLZTO. Since the stressed zone is significantly deeper than the typical defect size mechanically introduced cracks have been shown to be deflected perpendicular to the indentation direction. Finally, we demonstrated that the same is true for dendrites with respect to the penetration direction, which opens a new avenue to designing “dendrite-free” solid-state electrolytes for high-power and energy-dense solid-state batteries.

## 2. Results and Discussion

### 2.1. SRIM Simulation and Structural Profile

To identify the implantation conditions that allow the introduction of residual stresses in a depth up to 1  $\mu\text{m}$  in LLZTO we calculated the Ag implantation and damage profiles by kinetic Monte

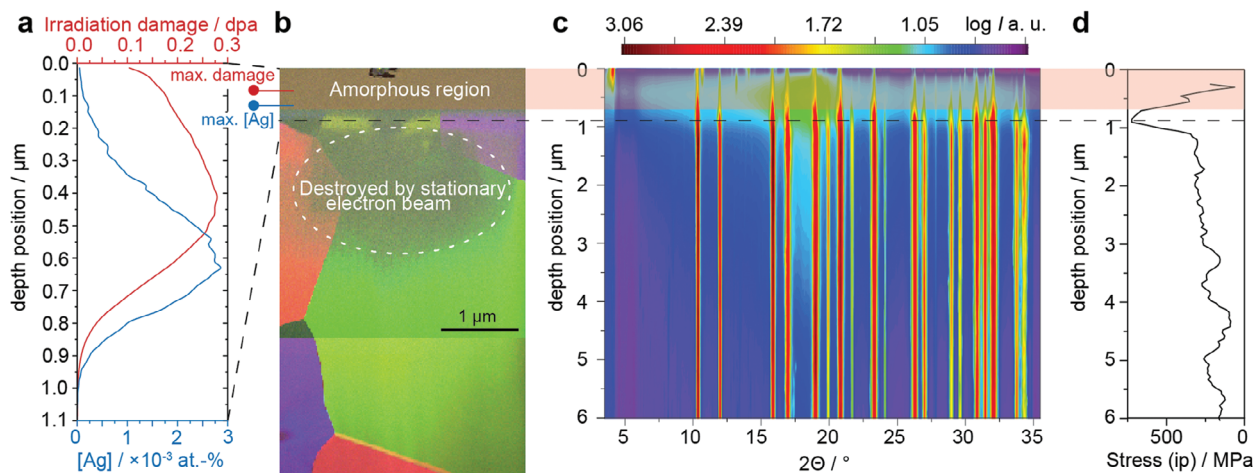


**Figure 1.** a) SRIM simulation of the damage and Ag ion distribution in  $\text{Li}_{6.4}\text{Ta}_{0.6}\text{La}_3\text{Zr}_{1.4}\text{O}_{12}$  crystal irradiated with 1.93 MeV Ag ions. b) SPED composite dark field image of a hot pressed  $\text{Li}_{6.4}\text{Ta}_{0.6}\text{La}_3\text{Zr}_{1.4}\text{O}_{12}$  polycrystal with Ag implanted into the top layer. An amorphous layer 650 nm deep is clearly visible. The material has also been shown to be particularly electron beam sensitive, being easily amorphized by the stationary electron beam between measurements. c) Compilation of cross-sectional nano X-ray diffraction patterns of the implanted polycrystalline LLZTO sample. The implanted region is shaded in orange. An amorphous region can be seen, starting from the surface down to a depth of 700 nm. Compressive in plane stress is shown in d) reaching a peak value of -700 MPa at 850 nm.

Carlo simulations with SRIM software (Figure 1a). It is shown that for implantation within 1  $\mu\text{m}$  a beam energy of 1.93 MeV has to be used. Both, the distribution of incorporated Ag ions as well as the associated damage caused by the irradiation can be estimated with a peak at  $630 \pm 30$  nm and at  $430 \pm 25$  nm for the amount of incorporated Ag ions and damage, respectively. With a dose of  $1 \times 10^{14}$  Ag-ions  $\text{cm}^{-2}$  an implanted concentration of 0.003 at% can be expected at the peak. There is the question of how accurate the simulation is when dealing with a polycrystalline ceramic, with possible chemical inhomogeneities. When predicting the ranges for single-crystalline silicon, it is rather precise with a slight overestimation of the range by 2–6 nm increasing with implantation energy.<sup>[32]</sup> For polycrystalline samples, in general, and for LLZTO specifically such studies are, to the best of our knowledge, not available.

In order to visualize potential changes in crystallinity Virtual Dark Field imaging was applied to a Scanning Precession Electron Diffraction (SPED) measurement of an implanted polycrystalline LLZTO sample as shown in Figure 1b. It reveals grain size in the range of 3–6  $\mu\text{m}$  and amorphization of LLZTO down to a depth of around  $650 \pm 10$  nm. This amorphization is also present in the FIB lamella before the TEM measurement, seen as a slightly differing contrast shown in Figure S1, Supporting Information. The region below shows indications of a mixed crystallinity, with amorphous regions dotting crystalline parts, though it is difficult to distinguish between amorphization caused by electron beam damage and the one stemming from ion implantation. This is in accordance with the Monte Carlo simulation and allows the assumption that a significant amount of the incorporated Ag could be detectable in a range from 550 to 750 nm for further measurements. Since structural degradation of LLZTO takes place even when using low beam current during SPED (see Figure S2, Supporting Information), atomic resolution imaging and locating the implanted Ag as well as the chemical analysis via energy dispersive X-ray spectroscopy (EDS) or

electron energy loss spectroscopy (EELS) has been hindered (attempted EDS and EELS results are shown in Figure 3a-e, Supporting Information).

Therefore, atom probe tomography (APT) analyses were performed at the peak implantation depth, around 700 nm, as well as after the peak damage, depth of 1300 nm. The noise level of the mass spectra under the chosen analysis conditions does, however, not allow to detect the low Ag content (around 0.003 at% at the peak of implantation based on SRIM simulation). In Figure 2a the 3D reconstruction of one of the three datasets obtained from a depth of 700 nm is shown which is representative for all of them. The atoms are homogeneously distributed throughout the needle and no grain boundaries are visible, meaning only a single grain was investigated. The chemical composition, shown in Table S1, Supporting Information, is close to the nominal composition of  $\text{Li}_{6.4}\text{La}_3\text{Zr}_{1.4}\text{Ta}_{0.6}\text{O}_{12}$ . Although, LLZTO is intended to be a single phase (see XRD, and electron microscopy analysis) the 3D reconstruction from a depth of 1300 nm on the other hand shows a clearly visible grain boundary, a grain with the same composition as in the previous dataset and a lithium deficient grain on top of it (Figure 2b). The lithium content in the upper grain is around  $10.4 \pm 2.0$  at.%, see Table S1, Supporting Information, while still having a homogeneous distribution of atoms. A proxigram from the grain boundary, Figure S4, Supporting Information, shows the transition in lithium content. There is also a dataset only containing a lower lithium content. The Li-poor extra phase could be related to minor extra phases which have already been present in the sample or to a lithium loss in the high vacuum conditions during the APT analysis, which has been recently demonstrated.<sup>[33,34]</sup>

Finally, we used focused ion beam-scanning electron microscopy (FIB-SEM) with correlative time of flight-secondary ion mass spectrometry (TOF-SIMS) to find evidence for the presence of Ag ions in the implanted zone. Figure 2c depicts the spots at the implantation zone near the edge and deeper in the sample

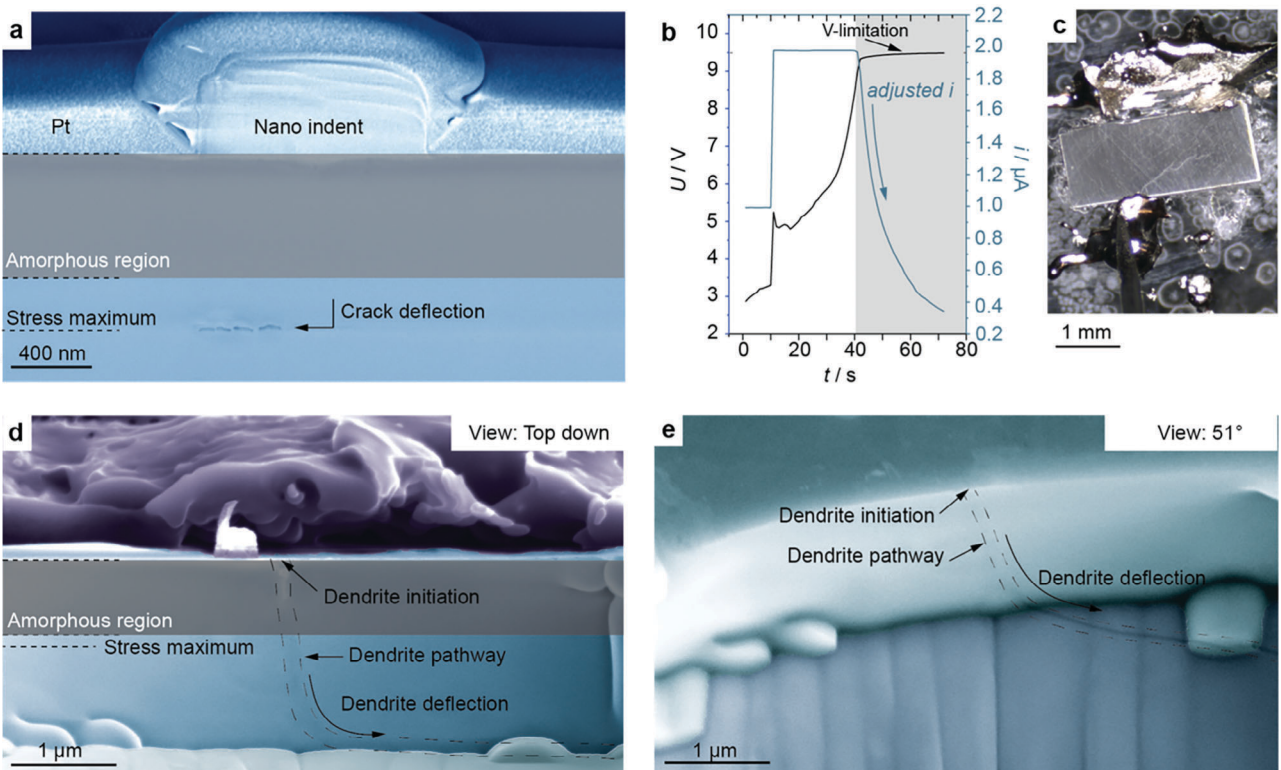


**Figure 3.** a) SEM image (Backscattered electrons) of a mechanically induced crack by nano indentation in Ag implanted single crystalline LLZTO. The crack grows preferably parallel to the surface. b) Voltage profiles during the short-circuiting measurement, spliced together. Current was doubled after 10s and held until the voltage limit was reached, likely due to void formation decreasing the contact area. c) Optical microscope image of the thinned hot pressed LLZTO during the short-circuit measurement. d,e) SEM image of an electrochemically induced crack in Ag implanted LLZTO. Top view (d) and 51° angled view (e). The implanted region is shaded in orange, and the crack highlighted with a dashed line. After the implantation zone, the crack diverts parallel to the surface.

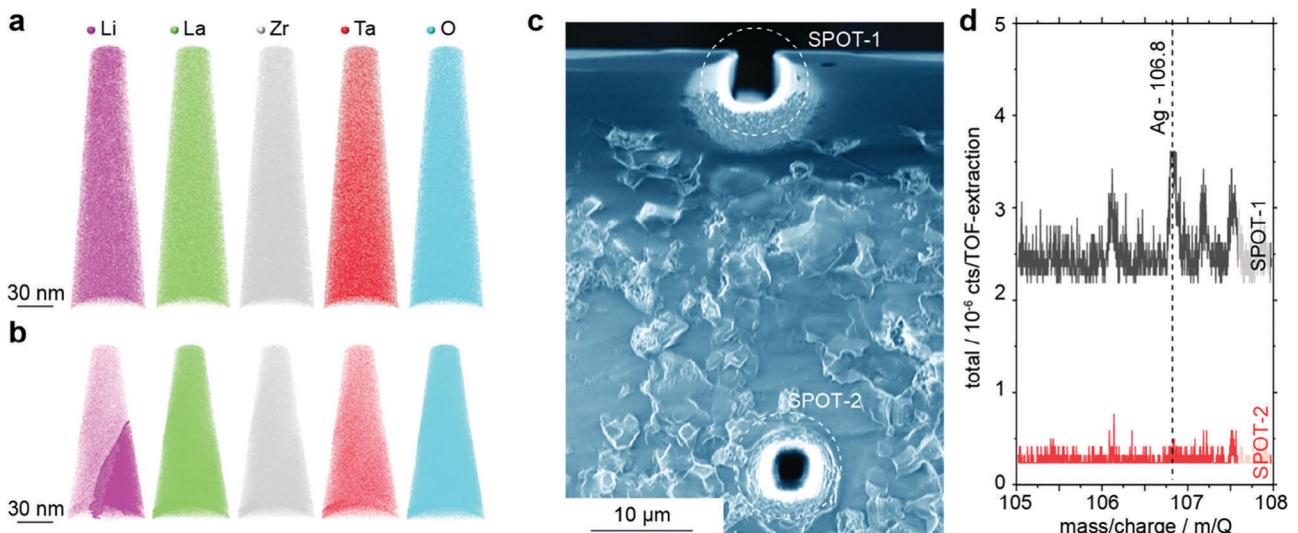


**Figure 2.** a) Atom probe tomography reconstruction of a needle prepared from a depth of 700 nm. The atoms are distributed homogeneously throughout the needle b) Reconstruction of a needle from a depth of 1300 nm. While there is still a homogeneous atom distribution within grains the lithium content in the upper part is lower. c) SEM image of the cross-section of the implanted LLZTO sample. The 2.5  $\mu\text{m}$  diameter spots are where TOF SIMS measurements were taken. d) TOF SIMS data from the two spots in (c). There is a slightly visible peak for  $^{107}\text{Ag}$  at 106.8 mass-to-charge ratio for the first spot at the edge. This peak vanishes for the other spot which is below the implanted region.

where the TOF SIMS measurements were taken. A slight peak, at 106.8 mass to charge ratio is visible in the first 2.5 μm diameter spot at the edge, which can be attributed to the <sup>107</sup>Ag implanted into this region. This peak vanishes deeper into the sample, shown in Figure 2d, confirming that the Ag is implanted into the desired depth. Attempts to, at least qualitatively, confirm the implantation profile using smaller spots, shown in Figure S5, Supporting Information, dropped the signal below the threshold where it is distinguishable from noise.

## 2.2. Stress Profile

To determine the localized strain of the LLZTO after implantation, scanning precession electron diffraction has been performed (Figure S6, Supporting Information). The diffraction patterns and the simulated patterns of LLZTO are generally in good agreement (see Figure S6b-c, Supporting Information), though some parts of the sample are only partially crystalline resulting in slightly divergent diffraction spots. Hence, the resolution of the electron diffraction spots has not been high enough to get reliable strain values.

Therefore, cross-sectional scanning nano XRD was used on a mechanically thinned sample to quantify the residual stress depth-profile created by the implanted ions. The 80 nm X-ray spot size allows the measurement of residual stresses and crystallinity with a high spatial resolution. The depth-dependent XRD patterns (Figure 1c) confirm a partial amorphization of the top 700 nm as indicated by the broad diffuse scattering peak centered around 18 ° 2θ and the inversely proportional decrease of reflections related to the LLZTO phase, as opposed to the underlying region below. From the orientation-dependent peak position, a depth-resolved residual stress profile (Figure 1d) can be calculated. At a depth of 850 nm below the surface, just below the amorphized layer, a compressive stress peak up to ≈700 MPa was evaluated, whereas throughout the rest of the layer the stress level does not exceed ≈250 MPa. The slight waviness of the residual stress depth profile is stemming from the fact that the recorded XRD patterns lie somewhere between those corresponding to a single-crystal and fully powder-like poly-crystal, resulting in residual stresses corresponding to the transition range between 1<sup>st</sup> and 2<sup>nd</sup> order stress, i.e., including some degree of grain-to-grain stress variation.

Based on this stress value and the methodology established in Fincher et al, it is possible to determine the flaw size of a dendrite that can be deflected with the present stress, similarly assuming that the compressive stress is responsible for the dendrite deflection.<sup>[14]</sup> Equation 1 is adapted from Fincher et al to determine the flaw size  $a$  and assumes a  $K_{IC} = 1 \text{ MPa m}^{1/2}$  for LLZO, same as in the reference due to using the same commercially acquired LLZTO, that our determined compressive stress at -700 MPa is 10% higher than the critical stress  $\sigma_{crit}$  to deflect all growing cracks to 90° giving a  $\sigma_{crit} = 636 \text{ MPa}$ .

$$a = \frac{(K_{IC})^2}{(1.12 * \sigma_{crit})^2 * \pi} = 627 \text{ nm} \quad (1)$$

From this, a flaw size of 627 nm is determined, which means that with the present stress of -700 MPa in a depth of 850 nm growing cracks should be deflected.

## 2.3. Proof of Concept: Deflection of Cracks

To test if crack deflection occurs with the implantation of Ag ions, Nanoindentation was used to probe the implanted region on a larger single crystalline LLZTO sample. The resulting crack propagation was observed in a FIB SEM cut (see Figure 3a and Figure S7, Supporting Information). Below the indentation imprint a crack runs parallel to the surface at a depth of 850 nm. This is as expected at the depth of the compressive stress zone, determined in the previous section. Notably absent are cracks connecting the indentation imprint and the fracture, which should be present if it is a radial fracture. Above the crack the amorphous region is again visible due to its differing contrast, additionally confirming the previous TEM and XRD results.

To prove the hypothesis that the implementation of stressed zones by ion implantation can also deflect dendrites we applied electrical current well above reported critical current densities to a thinned sample with Li metal on both sites until the voltage reached device limitations, as a result of reduced contact area from lithium stripping. The corresponding current-voltage curve is shown in Figure 3b. Figure 3c shows the setup used during this kind of short circuit testing, where the sample is contacted with lithium in two places, carefully applied only on the side, to avoid circumventing the implanted layer and the zone of compressive stress. It is evident from Figure 3d,e that dendrites deflect after the implanted region, similar to mechanically induced cracks. The deflection zone is somewhat past the stress maximum, determined at 850 nm, and the crack begins to kink at ≈700 nm and is fully deflected at 1.5 μm. Where the indented sample fractures at the zone of compressive stress, the growing dendrite has to snake its way through an increasing stress field, which can differ locally from the averaged values determined via XRD. Similarly, the bulk  $K_{IC}$  value can differ from  $K_{IC}$  value at lower length scales. With this it is entirely plausible for the crack to be fully deflected after the stress maximum, which is in agreement with Fincher et al, where it was shown that once the crack starts to kink and constant stress remains, it will eventually be turned by 90°.<sup>[14]</sup>

## 2.4. Impact on Electrical Properties

Since the damage caused by the ion beam and the change in the lattice from the differently sized ions implanted can have significant impact on the interfacial transport properties, electrochemical impedance spectroscopy (EIS) has been performed. In Figure 4 a Nyquist plot of a non-implanted LLZTO reference sample and an Ag-implanted sample can be seen. EIS of the Ag implanted LLZTO samples with non-blocking electrodes show the occurrence of a second semicircle as a result of the implantation procedure. This can be attributed to the now amorphized layer on both sides. The pristine hot-pressed sample was fitted with an equivalent circuit consisting of a resistor and a constant phase element (CPE) in parallel. A constant phase element was chosen instead of the capacitance as the semicircle is slightly depressed.

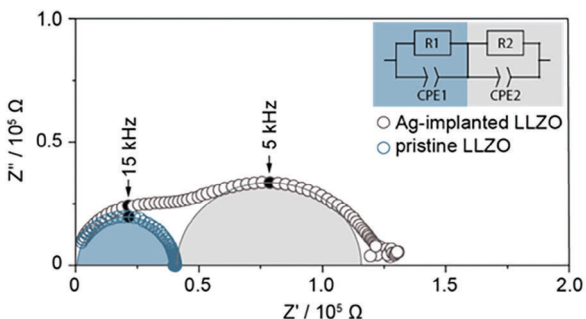


**Figure 4.** Nyquist plot of an Ag implanted (grey) and a non-implanted (blue) reference hot-pressed polycrystal. The equivalent circuits used to fit the arcs are shown in the top right corner. The second semicircle is attributed to the 650 nm amorphous layer which is detrimental to ionic transport as shown in previous literature.<sup>[26]</sup>

The calculated ionic conductivity is  $4.9 \times 10^{-4} \text{ S cm}^{-1}$ . Under the assumption that the bulk conductivity does not change and that the amorphous layer is symmetric on both sides the implanted sample was fitted with an equivalent circuit of two parallel R-CPE elements in series. The resulting ionic conductivity for the amorphous layer, calculated with the known thickness of 650 nm, is  $8.1 \times 10^{-8} \text{ S cm}^{-1}$ . This is in good agreement with already reported values for the ionic conductivity of amorphous LLZTO, which are in a similar order of magnitude.<sup>[27]</sup> The change in lattice structure hindering the lithium-ion transport. The original crystal structure could be regained by an annealing step, as it is typically used for doped semiconductors. The necessary parameters, how much it will broaden the implantation profile and the impact on the residual stress is not known yet for LLZTO and beyond the scope of this study.

### 3. Conclusion

In this study we investigated how Ag ions implanted into LLZTO affect crack growth, specifically induced by growing dendrites. First Ag ions were implanted in LLZTO using conditions determined by kinetic Monte Carlo simulations to introduce ions into a depth of up to 1  $\mu\text{m}$ , with a concentration peak at 750 nm. Determination of the actual concentration distribution and concentration maximum of the implanted ions was then attempted via APT and EELS. We found that the chosen dose of  $1 \times 10^{14} \text{ Ag ions cm}^{-2}$  resulted in an Ag concentration too low to quantify by these methods, so that a qualitative detection had to be achieved via TOF SIMS. Both spatially resolved cross-sectional nano XRD and SPED measurements revealed an amorphization of the region from the surface to a depth of 650 nm deep, partially also due to electron beam damage, which has been shown to be detrimental for the Li-ion conductivity. Moreover, from the corresponding X-ray diffractograms a compressive stress of up to  $-700 \text{ MPa}$  with its peak at a depth of 850 nm has been determined. Thereafter, the impact of the introduced stressed zone on the crack propagation has been evaluated. Cracks were induced in the material, mechanically via nanoindentation, and they indeed formed preferentially at the zone of compressive stress at 850 nm and parallel to the surface. Finally, it has been shown that electrochemically induced cracks (dendrites) can also be deflected, with the crack

beginning to kink at around 700 nm depth and fully deflecting slightly after the stress maximum at 1.5  $\mu\text{m}$ .

In summary, our results suggest that introduction of compressively pre-stressed zones in a depth exceeding the critical crack size, in addition with subsequent annealing steps for recrystallization of amorphous zones, could be a viable strategy to enable “dendrite-free” solid-state electrolytes to improve the rate-performance of solid-state batteries.

### 4. Experimental Section

**Sample Preparation:** The  $\text{Li}_{6.5}\text{La}_3\text{Zr}_{1.5}\text{Ta}_{0.5}\text{O}_{12}$  single crystal was pulled from a melt using the Czochralski technique. The thoroughly sintered initial material containing an excess of 20 Mol%  $\text{Li}_2\text{O}$  was melted in an inductively heated iridium crucible in pure Ar atmosphere and the crystal was pulled at a rate of 0.4 mm/h on a rotating seed oriented along [100]. The obtained crystal ingot was 15 mm in diameter and  $\approx 30$  mm long, mainly transparent of a slightly yellow color. The upper, first-grown part was covered by a thick film of opaque white material resulting from  $\text{Li}_2\text{O}$  depletion caused by evaporation. The hot-pressed polycrystals with the composition  $\text{Li}_{6.4}\text{Ta}_{0.6}\text{La}_3\text{Zr}_{1.4}\text{O}_{12}$  were acquired from commercial sources (Toshima). The single and polycrystals were cut into  $3 \times 3 \times 0.7$  mm cuboids. Two 0.7 mm sides parallel to each other were polished starting with SiC grinding paper with P1200, P2400 and P4000 grit size and final polishing using diamond paste of 3, 1, and 0.25  $\mu\text{m}$  particle size.

**Phase Purity Characterization:** For the commercial sample, the phase purity was checked via X-ray diffraction. The measurement was carried out on a Bruker Da-Vinci X-ray diffractometer using a  $\text{Cu K}\alpha$  source with a scanning window of  $10\text{--}60^\circ$  and a step size of  $0.013^\circ \text{ min}^{-1}$ , see Figure S8, Supporting Information.

**SRIM Simulation:** The damage in the  $\text{Li}_{6.4}\text{La}_3\text{Zr}_{1.4}\text{Ta}_{0.6}\text{O}_{12}$  sample, irradiated with 1.93 MeV Ag ions, was calculated using the SRIM-2013 software,<sup>[35,36]</sup> in full-cascade mode as recommended in Ref.[37] The density of  $\text{Li}_{6.4}\text{La}_3\text{Zr}_{1.4}\text{Ta}_{0.6}\text{O}_{12}$  was set to  $5.46 \text{ g cm}^{-3}$ . The threshold energies of displacement were set to 25 eV for Li, La, Zr, Ta, and 28 eV for O, according to literature.<sup>[38,39]</sup>

**Ion Implantation Procedure:** The samples were stacked in a stainless-steel sample holder and placed into a Pelletron implantation system type 3 SDH-2 NEC.  $^{107}\text{Ag}$  ions were implanted into both polished sides, flipping over after implantation of one side, with an energy of 1.930 MeV, a peak concentration of  $1 \times 10^{14} \text{ }^{107}\text{Ag}$  ions  $\text{cm}^{-2}$  ( $1 \times 10^{18} \text{ }^{107}\text{Ag}$  ions  $\text{cm}^{-3}$ ) and a current density of  $85 \text{ nA cm}^{-2}$ . The implanted samples were then put in 0.1 M HCl for around 20s followed by a rinse with Isopropanol and transferred to an Ar-filled glovebox ( $\text{O}_2$  and  $\text{H}_2\text{O} < 0.1 \text{ ppm}$ ) for storage and further experiments. Before any experiment, this HCl treatment was repeated to remove any  $\text{Li}_2\text{CO}_3$  layer formed during storage.

**Electrochemical Experiments:** The implanted sides of the cleaned samples were then coated with a molten  $\text{LiSn}$  alloy, containing 20 wt.% of Sn. The impedance of the coated samples was measured with a Solartron Modulab XM at  $25 \pm 1^\circ\text{C}$  with a perturbation voltage of 10 mV from 1 MHz to 10 Hz, 19 datapoints per decade of frequency after a 1 min OCV period. For the creation of dendrites, a current of up to  $1 \text{ mA cm}^{-2}$  was applied for 1 minute at  $25 \pm 1^\circ\text{C}$ . All measurements were performed in an Ar filled glovebox with  $\text{O}_2$  and  $\text{H}_2\text{O}$  levels below 0.1 ppm.

**TEM/SPED:** The  $\text{Li}_{6.4}\text{La}_3\text{Zr}_{1.4}\text{Ta}_{0.6}\text{O}_{12}$  sample was extracted from an Ar glovebox (10 min air exposure) and a 0.5  $\mu\text{m}$  layer of Ti was deposited on the Ag-implanted surface using an AJA electron beam evaporator. This protects against moisture from the air and carbon-containing deposition layers. A lamella was produced and thinned using the standard focused ion beam (FIB) liftout method, with a FEI Helios G4 UX dual-beam instrument. The final thinning was done using 2 kV Ga ions. The lamella was moved to a JEOL 2100F transmission electron microscope within 15 min air exposure.

Scanning precession electron diffraction was conducted using a precession angle of 0.8° and a frequency of 100 Hz. 20 ms diffraction patterns were acquired with a MerlinEM direct electron detector. Virtual dark-field imaging was used to separate grains and crystalline/amorphous areas.

**APT:** The tips for APT analysis were prepared from a lamella that was lifted out from the Ti coated Specimen, flipped upside-down and welded to flat Si posts inside the FIB. In this way, the Ti surface coating acts as a buffer between the specimen and the carbon-containing welding material, and the apex of each tip could be formed at a controlled distance from the original surface. The tips were formed using annular Ga ion milling, finishing with 2 kV for the final sharpening.

The APT measurements were carried out on a LEAP 5000 XS from CAMECA equipped with a UV laser. The specimen temperature was set to 60 K. Laser pulses with an energy of 20 to 30 pJ were used at a frequency of 200 kHz to trigger field evaporation. The standing voltage was automatically adjusted by the software to maintain a detection rate of 0.3% ions per pulse.

The commercial software IVAS from CAMECA was used for the reconstruction and analysis of the APT data. The reconstructed volumes were built using tip-profile reconstruction using secondary electron images obtained during specimen preparation by FIB.

**TOF SIMS:** The time-of-flight secondary ion mass spectroscopy measurement was carried out on a Helios PFIB instrument using Xe ions at 30 kV for analysis.

**CS-Nano XRD:** For the Synchrotron measurements two implanted  $\text{Li}_{6.4}\text{La}_3\text{Zr}_{1.4}\text{Ta}_{0.6}\text{O}_{12}$  polycrystalline sample cross-sections were thinned down to a final thickness of around 80  $\mu\text{m}$  by conventional mechanical polishing as mentioned above. The cross-sectional scanning X-ray nanodiffraction (CSnanoXRD) experiment was carried out at the nanofocus end station of the Microfocus beamline ID13 at the European Synchrotron Radiation Facility (ESRF) in Grenoble, France.<sup>[40]</sup> The sample was scanned by a monochromatic X-ray beam of 13 keV photon energy focused to  $\approx 80$  nm spot size by multi-layer Laue lenses, applying a scanning step of 50 nm in the direction perpendicular to the implanted surface.<sup>[41]</sup> 40 depth-profile scans spaced 1  $\mu\text{m}$  apart were averaged in order to counteract the poor diffraction statistics that result from the combination of small X-ray beam, thin sample slice, and comparatively large grain size of the probed material. Diffraction patterns were acquired in transmission on a Dectris Eiger X 4 M two-dimensional (2D) X-ray detector placed 10.98 cm downstream of the sample with an exposure time of 50 ms. The exact detector position was calibrated by measuring a standard corundum reference powder, using the routines provided by the pyFAI software package.<sup>[42]</sup> 2D diffraction patterns in the form of Debye-Scherrer rings were integrated azimuthally using the pyFAI software package and subsequently processed using custom python scripts for peak fitting with Pseudo-Voigt functions and strain/stress calculation. The evaluation of stress was based on the plausible assumption that there is no force acting perpendicularly on the free surface of the sample, which makes the application of a  $\sin^2\psi$ -based method possible. In such a case, the only necessary input parameters are the elastic properties of the probed material, i.e., in this case, the X-ray elastic constant  $\frac{1}{2}S_2$ , which was calculated for the relevant X-ray reflection {3̄12} from literature single-crystal elastic values using in a Hill grain interaction model, as  $\frac{1}{2}S_2,_{\text{LLZO}} = 7.831 \cdot 10^{-6} \text{ MPa}^{-1}$ . In summary, the CSnanoXRD experiment and the applied evaluation technique correspond to earlier studies of thin film samples at the same beamline, for more details see Ref. [43].

**Nanoindentation:** An implanted single crystalline  $\text{Li}_{6.4}\text{La}_3\text{Zr}_{1.4}\text{Ta}_{0.6}\text{O}_{12}$  sample was placed in a FT-NMT03 nanomechanical testing system utilized within a Cross Beam 340 ZEISS SEM. Indents are controlled by displacement and were made using a Berkovich indenter tip with an indentation depth of 0.1  $\mu\text{m}$ .

After attaching a few  $\mu\text{m}$  of Pt protection layer a  $20 \times 12 \times 10 \mu\text{m}$  cross section was cut with FIB using a 20 nA beam current, reduced to 4 nA and 600 pA for final polishing on a cross-beam SEM from Zeiss (AU-RIGA – CrossBeam workstation). The Image in Figure 3a was taken with

an acceleration voltage of 2 kV and performed in backscattered electron mode.

## Supporting Information

Supporting Information is available from the Wiley Online Library or from the author.

## Acknowledgements

D.R. acknowledges financial support by the Austrian Federal Ministry for Digital and Economic Affairs, the National Foundation for Research, Technology and Development and the Christian Doppler Research Association (Christian Doppler Laboratory for Solid State Batteries). The authors would like to thank Markus Stypa for assistance in crystal growth and acknowledge the European Synchrotron Radiation Facility (ESRF) for the provision of synchrotron radiation facilities and would like to thank Manfred Burghammer for assistance and support in using beamline ID13. The Research Council of Norway (RCN) is acknowledged for the support to the Norwegian Micro- and Nano-Fabrication Facility, NorFab, project number 295864, the Norwegian Laboratory for Mineral and Materials Characterization, MiMaC, project number 269842/F50, and the Norwegian Center for Transmission Electron Microscopy, NORTEM (197405/F50). The authors D.R. R.B and B.S gratefully acknowledge the financial support under the scope of the COMET program within the K2 Center “Integrated Computational Material, Process and Product Engineering (IC-MPPE)” (Project No 886385) within the project ASSESS P1.10. This program is supported by the Austrian Federal Ministries for Climate Action, Environment, Energy, Mobility, Innovation and Technology (BMK) and for Labour and Economy (BMAW), represented by the Austrian Research Promotion Agency (FFG), and the federal states of Styria, Upper Austria and Tyrol.

## Conflict of Interest

The authors declare no conflict of interest.

## Author Contributions

F.F. and L.P. performed the experimental work, S.G. synthesized the single crystals. V.B. performed the ion implantation. S.W. performed the FIB cuts, SPED measurements, and APT needle preparation. H.S.S performed the APT analysis under supervision of Y.L. with the help of C.H.. C.H performed the SRIM simulation and APT data treatment and interpretation. B.S. and R.B. performed the nanoindentation. J.T. performed the CS nano XRD measurement with help from M.B., J.K, L.P., and D.R.. D.R. supervised the work. F.F., L.P., and D.R. wrote the first draft of the manuscript. All authors contributed to the final draft.

## Data Availability Statement

The data that support the findings of this study are available from the corresponding author on reasonable request.

## Keywords

dendrites, ion implantation, LLZO, solid electrolytes, solid-state batteries

Received: September 29, 2023

Published online:

- [1] M. V. Reddy, A. Mauger, C. M. Julien, A. Paolella, K. Zaghib, *Materials* **2020**, *13*, 1884.
- [2] W. Xu, J. Wang, F. Ding, X. Chen, E. Nasybulin, Y. Zhang, J.-G. Zhang, *Energy Environ. Sci.* **2014**, *7*, 513.
- [3] J.-M. Tarascon, M. Armand, *Nature* **2001**, *414*, 359.
- [4] D. Lin, Y. Liu, Y. Cui, *Nat. Nanotechnol.* **2017**, *12*, 194.
- [5] S. Yu, R. D. Schmidt, R. Garcia-Mendez, E. Herbert, N. J. Dudney, J. B. Wolfenstine, J. Sakamoto, D. J. Siegel, *Chem. Mater.* **2016**, *28*, 197.
- [6] F. Han, Y. Zhu, X. He, Y. Mo, C. Wang, *Adv. Energy Mater.* **2016**, *6*, 1501590.
- [7] E. J. Cheng, A. Sharafi, J. Sakamoto, *Electrochim. Acta* **2017**, *223*, 85.
- [8] Y. Ren, Y. Shen, Y. Lin, C.-W. Nan, *Electrochem. Commun.* **2015**, *57*, 27.
- [9] F. Flatscher, M. Philipp, S. Ganschow, H. M. R. Wilkening, D. Rettenwander, *J. Mater. Chem.* **2020**, *8*, 15782.
- [10] C.-L. Tsai, V. Roddatis, C. V. Chandran, Q. Ma, S. Uhlenbruck, M. Bram, P. Heijmans, O. Guillon, *ACS Appl. Mater. Interfaces* **2016**, *8*, 10617.
- [11] L. Porz, T. Swamy, B. W. Sheldon, D. Rettenwander, T. Frömling, H. L. Thaman, S. Berendts, R. Uecker, W. C. Carter, Y.-M. Chiang, *Adv. Energy Mater.* **2017**, *7*, 1701003.
- [12] J. Kasemchainan, S. Zekoll, D. Spencer Jolly, Z. Ning, G. O. Hartley, J. Marrow, P. G. Bruce, *Nat. Mater.* **2019**, *18*, 1105.
- [13] T. Krauskopf, H. Hartmann, W. G. Zeier, J. Janek, *ACS Appl. Mater. Interfaces* **2019**, *11*, 14463.
- [14] C. D. Fincher, C. E. Athanasiou, C. Gilgenbach, M. Wang, B. W. Sheldon, W. C. Carter, Y.-M. Chiang, *Joule* **2022**, *6*, 2794.
- [15] Q. Yue, C. Ban, S. J. Harris, *Joule* **2020**, *4*, 2599.
- [16] A. D. Rollett, U. F. Kocks, *Solid State Phenom.* **1993**, *35*, 1.
- [17] M. Kobayashi, T. Matsui, Y. Murakami, *Int. J. Fatigue* **1998**, *20*, 351.
- [18] A. Gujba, M. Medraj, *Materials* **2014**, *7*, 7925.
- [19] R. K. Chintapalli, A. Mestra Rodriguez, F. Garcia Marro, M. Anglada, *J. Mech. Behav. Biomed. Mater.* **2014**, *29*, 126.
- [20] I. Altenberger, in *Conf. Proc: ICSP*, IITT International, Paris, **2005**, *9*, 144–155.
- [21] P. P. Shukla, P. T. Swanson, C. J. Page, *Proc. Inst. Mech. Eng., Part B* **2014**, *228*, 639.
- [22] J. Pelleg, *Mechanical properties of ceramics*, Springer Science & Business, Switzerland, **2014**, Vol. 213. pp. 351–414.
- [23] J. S. Williams, *Mater. Sci. Eng.* **1998**, *253*, 8.
- [24] P. J. Burnett, T. F. Page, *Radiat. Eff.* **1986**, *97*, 283.
- [25] C. J. McHargue, *InDefect and Diffusion Forum*, Trans Tech Publications Ltd, Switzerland, **1988**, Vol. 57, pp. 359.
- [26] V. N. Gurarie, P. H. Otsuka, D. N. Jamieson, S. Prawer, *Nucl. Instrum. Methods Phys. Res. B* **2006**, *242*, 421.
- [27] S. J. Pearton, *Int. J. Mod. Phys. B* **1993**, *7*, 4687.
- [28] J. Sastre, M. H. Futscher, L. Pompizi, A. Aribia, A. Priebe, J. Overbeck, M. Stiefel, A. N. Tiwari, Y. E. Romanyuk, *Commun. Mater.* **2021**, *2*, 76.
- [29] G. A. Tarnavsky, E. V. Vorozhtsov, *Energy Power Eng.* **2010**, *2*, 73.
- [30] X. Yao, E. Olsson, M. Wang, J. Wang, Q. Cai, N. Peng, R. Webb, Y. Zhao, *Small* **2022**, *18*, 2108124.
- [31] H. Gao, X. Ai, H. Wang, W. Li, P. Wei, Y. Cheng, S. Gui, H. Yang, Y. Yang, M.-S. Wang, *Nat. Comm.* **2022**, *13*, 5050.
- [32] M. Titze, J. L. Pacheco, T. Byers, S. B. Van Deusen, D. L. Perry, D. Weathers, E. S. Bielejec, *J. Vac. Sci. Technol. A: Vac. Surf. Films.* **2021**, *39*, 063222.
- [33] O. Cojocaru-Mirédin, J. Schmieg, M. Müller, A. Weber, E. Ivers-Tiffée, D. Gerthsen, *J. Power Sources* **2022**, *539*, 231417.
- [34] S.-H. Kim, S. Antonov, X. Zhou, L. T. Stephenson, C. Jung, A. A. El-Zoka, D. K. Schreiber, M. Conroy, B. Gault, *J. Mater. Chem.* **2022**, *10*, 4926.
- [35] J. F. Ziegler, M. D. Ziegler, J. P. Biersack, *Nucl. Instrum. Methods Phys. Res. B* **2010**, *268*, 1818.
- [36] J. F. Ziegler, SRIM-2003, *Nuclear Instruments and Methods in Physics Research Section B: Beam Interactions with Materials and Atoms* **2003**, *219*, 1027.
- [37] W. J. Weber, D. M. Duffy, L. Thomé, Y. Zhang, *Curr. Opin. Solid State Mater. Sci.* **2015**, *19*, 1.
- [38] F. X. Zhang, G. Velisa, H. Xue, N. Sellami, C. Trautmann, Y. Zhang, W. J. Weber, *J. Condens. Matter Phys.* **2021**, *33*, 185402.
- [39] L. Pang, M. Cui, T. Shen, X. Gao, K. Wei, P. Tai, C. Yao, H. Chang, P. Jin, Z. Wang, *Results Phys* **2021**, *22*, 103861.
- [40] D. Rettenwander, J. Keckes, J. Todt, L. Porz, M. Meindlhummer, P. Gawlitza, S. Niese, “Scanning and In-situ MLL Development for X-ray Nanodiffraction on Thin Film, Space and Additively Manufactured Applications” [Data set]. European Synchrotron Radiation Facility, **2025**, <https://doi.org/10.15151/ESRF-ES-644167190>.
- [41] A. Kubec, K. Melzer, J. Gluch, S. Niese, S. Braun, J. Patommel, M. Burghammer, A. Leson, *J. Synchrotron Radiat.* **2017**, *24*, 413.
- [42] G. Ashiotis, A. Deschildre, Z. Nawaz, J. P. Wright, D. Karkoulis, F. E. Picca, J. Kieffer, *J. Appl. Crystallogr.* **2015**, *48*, 510.
- [43] J. Keckes, R. Daniel, J. Todt, J. Zalesak, B. Sartory, S. Braun, J. Gluch, M. Rosenthal, M. Burghammer, C. Mitterer, S. Niese, A. Kubec, *Acta Mater.* **2018**, *144*, 862.